Journal of Materials Chemistry A

Mixed Ionic-electronic Conductivity of High-nickel, Single-crystal Cathodes Influencing the Cycling Stability of All-solid-state Lithium-ion Batteries

Journal:	*Journal of Materials Chemistry A*
Manuscript ID	TA-ART-05-2024-003727.R1
Article Type:	Paper
Date Submitted by the Author:	23-Aug-2024
Complete List of Authors:	Lee, Steven; The University of Texas at Austin Lee, Dongsoo; The University of Texas at Austin Manthiram, Arumugam; The University of Texas at Austin, Materials Science and Engineering

ARTICLE

Mixed Ionic-electronic Conductivity of High-nickel, Single-crystal Cathodes Influencing the Cycling Stability of All-solid-state Lithium-ion Batteries

Received 00th January 20xx,
Accepted 00th January 20xx

DOI: 10.1039/x0xx00000x

Steven Lee, Dongsoo Lee, and Arumugam Manthiram*

High-nickel, cobalt-free layered oxides are emerging as promising cathode materials for traditional lithium-ion batteries (LIBs), but their application in all-solid-state batteries (ASSBs) remains largely unexplored. This study benchmarks the electrochemical properties of single-crystal $LiNi_{0.8}Co_{0.2}O_2$ (SC-NC80) and cobalt-free $LiNi_{0.8}Mn_{0.2}O_2$ (SC-NM80) in both conventional LIBs with liquid electrolytes and in ASSBs. While SC-NM80 displays inferior electronic conductivity and lithium diffusion kinetics, its cycling stability in conventional LIBs is improved relative to SC-NC80, owing to the stability provided by redox-inactive Mn^{4+} in the layered structure. Despite such benefits, the kinetic limitations of SC-NM80 become problematic for the cycling stability of ASSBs with a poor electronic percolating network in the cathode composite. Conductivity measurements demonstrate the negative impact of reduced cathode mixed ionic-electronic conductivity on the effective transport properties within the cathode composite for ASSBs. Insufficient electronic conductivity in the cathode composite induces lithiation inhomogeneity at a moderate C/3 rate, leading to severe active material (AM) loss at low states-of-charge (SOC). This study reveals the intrinsic challenges of incorporating Co-free cathodes in ASSBs and underscores the necessity for strategic electrode engineering to enhance the effective electronic conductivity of high-Ni, Co-free cathode composites.

Introduction

The geographical scarcity and human rights concerns associated with cobalt mining are driving the battery industry to eliminate cobalt from cathode materials to enhance the long-term sustainability of lithium-ion batteries (LIBs).[1] Despite the challenge of forming an ordered layered structure formation with cobalt, cobalt-free cathode compositions, such as $LiNi_xMn_yAl_zO_2$ (NMA, $x \geq 70\%$), $LiNi_{0.93}Al_{0.05}Mg_{0.01}Ti_{0.01}O_2$, $LiNi_{0.96}Mg_{0.02}Ti_{0.02}O_2$, and $LiNi_{0.96}Mn_{0.02}Mg_{0.02}O_2$, have demonstrated promising electrochemical stabilities and comparable rate capabilities, suggesting cobalt may not be needed in high-energy cathode materials.[2–8] Nevertheless, high-Ni cathodes generally suffer from parasitic reactions at the cathode-electrolyte interface during high-voltage or high-temperature operations, leading to active material (AM) loss and accelerating capacity fade.[9–11] To address these issues, single-crystal high-Ni cathodes have been shown to mitigate cathode reactivity issues and extend battery cycle life by reducing electrochemically active surface area and resisting particle cracking compared to their polycrystalline counterparts, making them a critical area of research for next-generation high-energy cathode materials.[12–19]

Materials Science and Engineering Program, Texas Materials Institute, The University of Texas at Austin, Austin, TX, 78712-1591, USA. E-mail: rmanth@mail.utexas.edu

Electronic Supplementary Information (ESI) available: [details of any supplementary information available should be included here]. See DOI: 10.1039/x0xx00000x

Aside from single-crystal cathodes, all-solid-state batteries (ASSBs) hold immense promises as the new frontier for next-generation LIBs, enabling higher energy density cells with lithium-metal anodes and improved safety with non-flammable inorganic solid electrolytes. However, the commercial adoption of high-energy density ASSBs has yet to be realized due to stringent cell engineering requirements. These include employing a high-capacity (> 200 mAh g^{-1}) high-Ni cathode with a high AM volume fraction (> 70 vol.%) and areal loading (> 5 mAh cm^{-2}) in the cathode composite, an ultra-thin solid electrolyte separator layer (< 30 μm), and an anode-free architecture. Additionally, ASSBs must achieve similar capacity retention compared to conventional LIBs (~ 80% retention over 1,000 cycles) under moderate cell stack pressure, a formidable task that has yet to be demonstrated on a commercial scale.[20] This necessitates not only robust electrochemical stabilities in both the cathode and anode, but also substantial cell manufacturing prowess with robust quality assurance processes to eliminate separator defects that can lead to catastrophic cell failure.[21]

Achieving prolonged cycle life on the cathode side of ASSBs is fundamentally challenging from a mechanochemical perspective. The well-known anisotropic volume contraction of many Ni-based layered oxides (regardless of Ni content) at high states-of-charge (SOC) is particularly detrimental to the cycle life of ASSBs, as the initially intimate interfacial contacts, critical for facile ionic transport, are disrupted with repeated cycling.[22–24] Primary particle contact within polycrystalline cathode particles can also become disconnected due to particle cracking,

leading to AM isolation and high impedance growth. Therefore, utilizing single-crystal cathodes is essential to eliminate internal grain boundaries and mitigate the high interparticle contact resistance growth in ASSBs.[25,26] Besides cathode morphological control, cathode compositions can also subtly influence the degree of volume change and its evolution as a function of SOC. For instance, a series of $LiNi_xMn_{(1-x)}O_2$ ($75 \leq x \leq 95$) cathodes exhibit a slightly lower volume change compared to $LiNi_{0.9}Co_{0.1}O_2$ under the same SOC, underscoring the benefit of Mn^{4+} in reducing lattice distortion at deep delithiation states.[27] This suggests that an appropriate $LiNi_xMn_{(1-x)}O_2$ composition with a single-crystal morphology can be an attractive high-capacity cathode material for ASSBs with reduced mechanical instability. Combined with the concerted effort to eliminate cobalt from cathode materials, understanding the effects of utilizing a Co-free single-crystal cathode in ASSBs is warranted. Unfortunately, most ASSB research focuses on single-crystal $LiCoO_2$, $LiNi_{0.6}Mn_{0.2}Co_{0.2}$ (NMC-622), or $LiNi_{0.8}Mn_{0.1}Co_{0.1}O_2$ (NMC-811) as cathode materials, and not enough attention is given towards understanding the effect of cathode composition on the performance of ASSBs.

In this study, the electrochemical properties of single-crystal $LiNi_{0.8}Co_{0.2}O_2$ (SC-NC80) and $LiNi_{0.8}Mn_{0.2}O_2$ (SC-NM80) are compared in conventional coin cells with a liquid electrolyte and in ASSBs to evaluate the viability of Co-free cathodes in ASSBs. We employ morphological and crystallographic characterization of the pristine cathode materials, alongside cycle life testing, lattice volume change measurement, and kinetic characterization in conventional coin cells, to identify the fundamental cathode properties conducive to the cyclability of ASSBs. By integrating these key insights with fundamental cathode chemistry knowledge, we uncover the technical hurdles of incorporating Co-free cathodes in ASSBs, shedding light on potential strategies to overcome these challenges to effectively deploy Co-free cathodes.

Experimental

Materials Synthesis

Cathodes. Single-crystal $LiNi_{0.8}Co_{0.2}O_2$ (SC-NC80) and $LiNi_{0.8}Mn_{0.2}O_2$ (SC-NM80) were synthesized with a molten-salt high-temperature calcination method. $Ni_{0.8}Co_{0.2}(OH)_2$ or $Ni_{0.8}Mn_{0.2}(OH)_2$ was mixed with LiOH·H2O (Alfa Aesar, 99.995%) and Na_2SO_4 (Sigma Aldrich, 99%) in a 1 : 1.1 : 1 mole ratio or with LiOH·H2O, Na_2SO_4, and Li_2SO_4 (Sigma Aldrich, 99.5%) in a mole ratio of 1 : 1.1 : 0.9 : 0.1, respectively, in a mortar and pestle. The mixture was calcined in a tube-furnace with flowing O_2 at 500 °C for 5 h then 820 °C for SC-NC80 and 900 °C for SC-NM80 for 6 h, followed by rinsing with H_2O to remove the sulfate molten salt and filtering to extract the cathode powders. After drying in a 110 °C oven, the cathode powders were mixed with 3 mol% of LiOH and annealed again in a tube-furnace with flowing O_2 at 740 °C for SC-NC80 and 810 °C for SC-NM80 for 1 h to obtain the final cathode materials.

Solid electrolytes. Li_3InCl_6 (LIC) was synthesized through a mechanochemical reaction followed by annealing. A mixture of anhydrous LiCl (99.9%, Sigma-Aldrich) and $InCl_3$ (99.999%, Sigma-Aldrich) in a 3 : 1 mole ratio was ball milled in a ZrO_2 milling jar with 10 mm ZrO_2 balls at 500 rpm for 20 h. Afterward, the mixture was heat-treated at 270 °C for 6 h in an Ar atmosphere and was ball-milled again with 3 mm ZrO_2 balls at 300 rpm for 6 h to reduce the particle size. The ionic conductivity was 0.86 mS cm^{-1} (Fig. S1). $Li_{5.5}PS_{4.5}Cl_{1.5}$ (LPSCl) was synthesized through a similar process as LIC, except a mixture of Li_2S (99.9%, Sigma-Aldrich), P_2S_5 (99.99%, Sigma-Aldrich), and anhydrous LiCl in a 2 : 0.5 : 1.5 mole ratio was ball milled and subsequently heat-treated at 500 °C for 5 h in an Ar atmosphere. The ionic conductivity was 2.25 mS cm^{-1} (Fig. S1).

Materials characterization

The morphologies of the single-crystal cathode samples were observed with a Scios 2 DualBeam (Thermo Scientific) focused ion beam scanning electron microscope (FIB-SEM) with a 2 kV electron beam. The cathode surface area was determined by an N_2 physisorption method with a Micromeritics TriStar II Plus 3030 surface area analyzer, and the surface area values were calculated according to the Brunauer-Emmett-Teller (BET) theory. The crystal structure of the cathode samples was probed with X-ray diffraction (XRD) in a Rigaku Miniflex 600 diffractometer. The diffraction patterns were collected at a 2θ range of 10 – 80° in 1 hour with Cu Kα radiation (λ = 1.54184 Å). Rietveld refinement was performed with FullProf. Details on the refined parameters can be found in our previous work.[28] For measuring the cathode lattice volume change, the cathode electrodes were charged to 4.4 V without formation cycling. The electrodes were extracted from the half cell and rinsed several times with dimethyl carbonate (DMC, Sigma-Aldrich). After drying under vacuum, the electrodes were placed into an air-sensitive XRD sample holder and were characterized with XRD. Several experimental steps were taken to eliminate peak position variations due to sample height differences between each measurement. First, the shift in the XRD pattern of the pristine electrode was eliminated by matching it to the XRD pattern of the cathode powder within the same sample batch. Then, the Al peak in the XRD pattern of the pristine electrode was used as the reference peak for the XRD pattern of the cycled electrode. Lining up the Al peaks would ensure a fair comparison between the pristine and cycled electrodes with decent peak position accuracy. The lattice constants were calculated based on the peak location of the (003) peak and (110) peak for *c* and *a* lattice parameter, respectively.

Cell preparation

Conventional coin cells. In conventional coin cell testing with a liquid electrolyte, cathode electrodes were fabricated by incorporating the single-crystal cathodes, Super C65 carbon black (Imerys), and Kynar HSV 1810 polyvinylidene fluoride (PVDF) (Arkema) in a weight ratio of 90 : 5 : 5 into a slurry with N-methyl-2-pyrrolidinone (NMP, > 99%, Sigma-Aldrich), followed by rigorous mixing in a planetary mixer (Thinky AR-100) and tape-casting onto an Al foil (15 μm, MTI Corp.). The

loading is around 5.5 mg cm^{-2}, corresponding to an areal capacity of around 1 mAh cm^{-2}. The electrodes were calendered to a press density of 3.0 g cm^{-3} and dried overnight in a vacuum oven at 110 °C. 2032-type coin cells were fabricated inside an Ar-filled glovebox with a 12-mm cathode electrode disc, Celgard 2325 separator, Li-metal anode (AOT Battery), and LP57 electrolyte (Gotion). The LP57 electrolyte comprised 1.0 M lithium hexafluorophosphate ($LiPF_6$) in ethylene carbonate (EC) and ethyl methyl carbonate (EMC) (3:7 by weight).

All-solid-state batteries (ASSBs). The single-crystal cathode materials were incorporated into dry electrodes with LIC, vapor grown carbon fibers (VGCF, Sigma-Aldrich), and PTFE (Sigma-Adrich) in a weight ratio of 60 : 37 : 2 : 1 for 60% AM loading and 70 ; 27 : 2 : 1 for 70% AM loading. The areal loading is around 3 – 4 mAh cm^{-2} after rolling out the dry electrode on a heated glass plate with a stainless-steel rod. ASSBs were assembled by first pressing the dry cathode composite, then 50 mg of LIC as an interlayer, and lastly 150 mg of LPSCl as a separator layer under 370 MPa of pressure in a solid-state battery setup. This setup consisted of a PEEK insert with a 12.7-mm diameter opening and two 17-4 stainless-steel rods. Finally, $Li_{0.5}In$ metal foil was attached to the LPSCl separator layer under a mild pressure to complete the ASSB assembly.

Conductivity cells. An ion-blocking solid-state cell was used to measure the electronic conductivity of the pure cathode samples and the cathode composite. Pure AMs with 2 wt.% PTFE or the same cathode composites used in ASSBs were pelletized to ~80% dense in the solid-state battery setup. Afterward, a soft carbon-coated Al foil (Toyal-Carbo) was pressed and attached to both sides of the pellet to eliminate interfacial contact resistance between the sample and the stainless-steel rods. An electron-blocking symmetric ASSB was constructed with the cathode composite in the middle to measure the ionic conductivity of the cathode composites. Specifically, the cathode composites were first pelletized, and then 150 mg of LPSCl were spread and pressed on both sides of the cathode composites. Finally, $Li_{0.5}In$ metal foil was attached to both sides of the LIC layer to achieve the symmetric ASSB.

Electrochemical characterization

For cycle life testing, both coin cell and ASSB testing were conducted at room temperature (~23 °C) with a 96-channel Arbin cycler from 2.8 to 4.4 V vs. Li (V_{Li}) at a C/3 rate (1C = 180 mA g^{-1}) after four C/10 formation cycles. All charging steps followed a constant current–constant voltage (CCCV) protocol until a current equivalent to C/20 rate was reached. The ASSBs operated with 20 MPa of external stack pressure inside an Ar-filled glove box. The operating voltage range was adjusted based on the difference between In and Li redox potential (~0.6 V). For the discharge rate testing in coin cells, the charging rate was at C/10 with the same CCCV protocol, and four discharge cycles of C/10, C/5, C/2, 1C, 2C, 5C, and 10C were conducted sequentially. A galvanostatic intermittent titration technique (GITT) measurement was performed in the discharge rate testing coin cells after four C/10 cycles. A 5-minute charge/discharge pulse were followed by a 10-minute rest in GITT until the same cut-off voltages (2.8 – 4.4 V_{Li}) were reached. The Li^+ diffusion coefficient (D_{Li^+}) was determined with the following equation:

$$D_{Li^+} = \frac{4}{\pi}\left(\frac{V}{A}\frac{\frac{\Delta E_{OC}}{\Delta t_I}}{\frac{dE}{d\sqrt{t}}}\right)^2 \quad (1)$$

where V is the molar volume of AM, A is the surface area of the AM, ΔE_{OC} is the change of open-circuit voltage after resting for Δt_I of 600 s, and $\frac{dE}{d\sqrt{t}}$ is the slope of voltage change after sustaining a pulse for 60 s. Please refer to this article for a detailed description of the GITT method and calculation.[29] Electronic conductivities of the AMs and the solid-state cathode composites were measured with a DC polarization method, where the samples were subjugated to five incremental voltage steps (10 – 50 mV for AM testing and 2 – 10 mV for cathode composite testing) and the steady-state current responses were recorded. The conductivity value was calculated with Ohm's law:

$$\sigma = \frac{L}{R \cdot S} \quad (2)$$

where L is the thickness of the pelletized sample, R is the resistance value deduced from the linear regression of the voltage-current profile, and S is the cross-sectional area of the solid-state battery setup (1.267 cm^2). Ionic conductivities of the solid-state electrolytes and the cathode composites were measured with electrochemical impedance spectroscopy (EIS, Biologic) with a 50-mV excitation amplitude from 1 MHz to 10 mHz. The resistance value was extracted by fitting the second

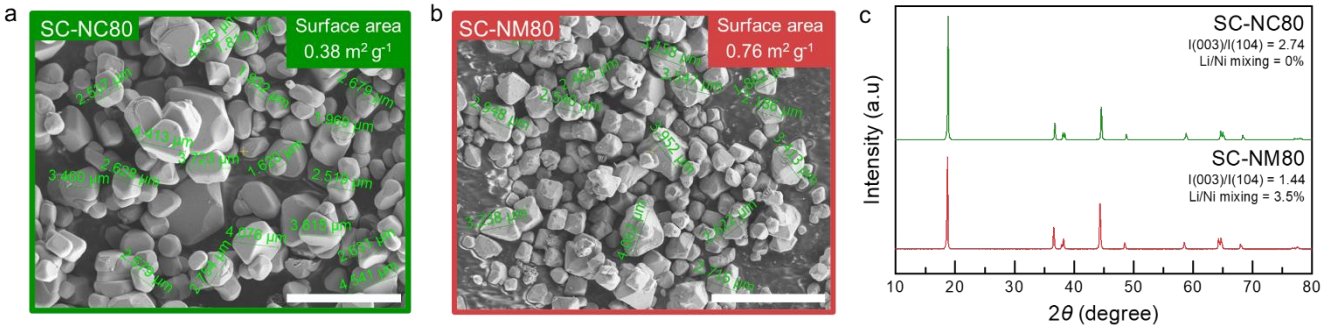

Fig. 1 Characterization of pristine single-crystal $LiNi_{0.8}Co_{0.2}O_2$ (SC-NC80) and $LiNi_{0.8}Mn_{0.2}O_2$ (SC-NM80). Scanning electron microscope (SEM) images of (a) SC-NC80 and (b) SC-NM80. The BET surface area value is shown at the top right corner. The scale bar is 10 µm. (c) XRD patterns of SC-NC80 and SC-NM80 with the I(003)/I(104) intensity ratio and Li/Ni mixing indicated.

semicircle according to Siroma et al., and the conductivity values were calculated using equation 2.[30]

Results and discussion

Morphological and crystallographic properties

The single-crystal $LiNi_{0.8}Co_{0.2}O_2$ (SC-NC80) and $LiNi_{0.8}Mn_{0.2}O_2$ (SC-NM80) cathodes were synthesized with a molten-salt high-temperature calcination method. The scanning electron microscope (SEM) images in Fig. 1a and Fig. 1b reveal their particle sizes ranging from 2 to 4 µm, which is an ideal size to mitigate intragranular stress at high SOC and promote high AM utilization in ASSBs.[24,31,32] This particle size is achieved by adjusting the calcination temperature and the molten salt composition. SC-NC80 calcined at 820 °C with equimolar of Na_2SO_4 yields the optimal particle size, while calcining at 840 °C leads to a larger particle size of 5 – 8 µm due increased Ostwald ripening at higher calcination temperatures (Fig. S2).[12] However, achieving optimal particle size for SC-NM80 is more challenging when using only Na_2SO_4 as the molten salt. Particle size distribution varies significantly with calcination temperature (Fig. S3). Specifically, SC-NM80 calcined at 870 and 900 °C result in abnormally large particle sizes of > 7 and 10 µm, respectively, while calcining at 850 °C yielded submicron particles. This sensitivity is likely related to the surface energy of various particle facets as a function of the cathode and molten salt compositions.[33,34] SC-NM80 calcined with Na_2SO_4 likely promotes surface facets with a high surface energy, leading to excessive grain growth. The varying surface faceting behavior between SC-NC80 and SC-NM80 can be visualized in Fig. S2 and Fig. S3, respectively. When calcined with Na_2SO_4, SC-NC80 exhibits a truncated octahedral morphology with rounded edges, while SC-NM80 exhibits a perfect octahedral morphology with sharp edges. Introducing a capping agent like Li_2SO_4 can reduce grain growth, as evidenced by SC-NM80 calcined at 900 °C with 0.9 : 0.1 mol ratio of Na_2SO_4 and Li_2SO_4, displaying an optimal particle size of 2 – 4 µm (Fig. 1b). The BET surface area of SC-NM80 is double that of SC-NC80 (0.76 vs. 0.38 $m^2\ g^{-1}$), likely indicating a higher proportion of smaller particles in SC-NM80.

The XRD patterns of the cathode samples display the typical diffraction pattern from the $R\bar{3}m$ space group and suggest a robust layered structure formation (Fig. 1c). Both cathodes exhibit a high I(003)/I(104) peak ratio, with SC-NC80 showing roughly double the peak ratio of SC-NM80. This is due to a combination of lower Li/Ni mixing in SC-NC80 (0%) compared to SC-NM80 (3.5%) and a higher preferred orientation of the (003) plane (Table S1 and S2). The formation of an ordered layered structure is expected for SC-NC80, since Co^{3+} is known to reduce magnetic frustration and promote cation ordering.[35,36] Preferred orientation of single-crystal cathode samples arises from the uniform orientation of the layered structure along the (003) plane, which indicates successful single crystal synthesis. Indeed, the preferred orientation in SC-NM80 leads to a stronger (003) peak compared to that of polycrystalline NM80 (PC-NM80, Fig. S4). In addition, the FWHM of (003) and (104) peaks are smaller for SC-NM80 compared to PC-NM80, suggesting larger average crystallite size and less variation in crystal orientation. Overall, the similar particle size and crystal structure of these cathode samples validate the quality of the single-crystal cathode synthesis procedure and facilitate a fair comparison of their electrochemical properties.

Electrochemical properties

Cycling performance in conventional coin cells. Fig. 2 illustrates the electrochemical performances of SC-NC80 and SC-NM80 in

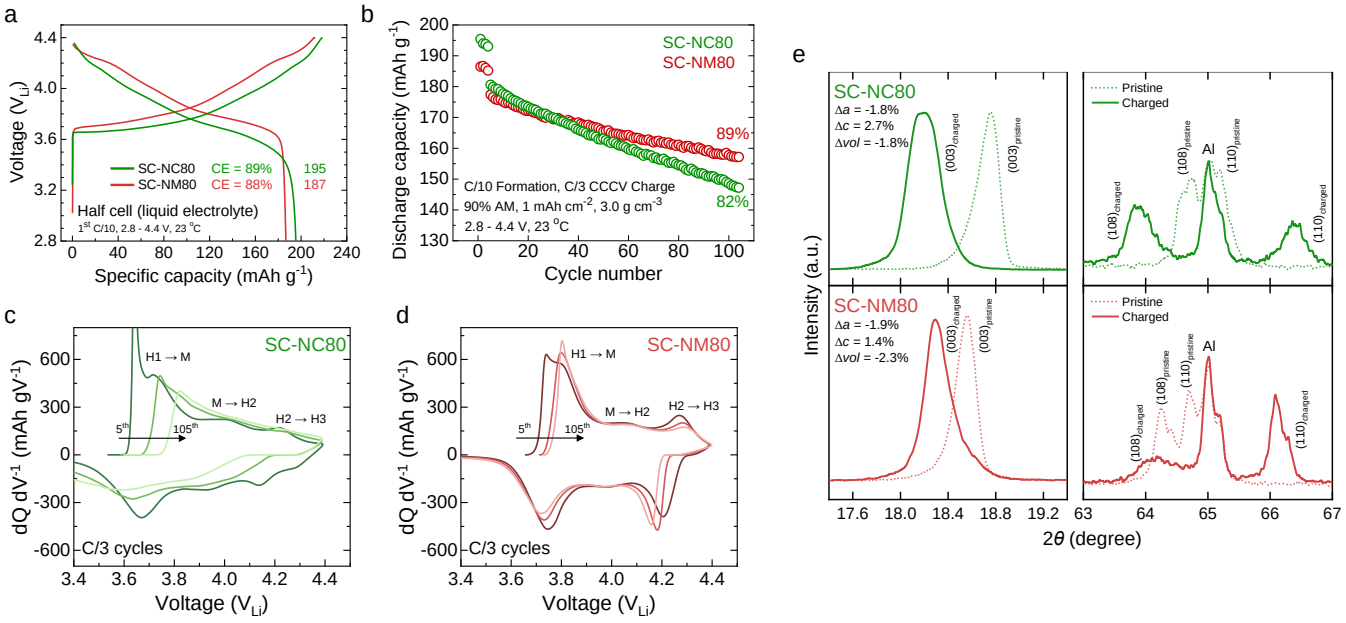

Fig. 2 Electrochemical characterization of SC-NC80 and SC-NM80. (a) 1st cycle voltage profile. (b) Cycling performance over 100 cycles at C/3 rate. (c, d) dQ dV^{-1} plots during C/3 cycling for (c) SC-NC80 and (d) SC-NM80. (e) *Ex-situ* XRD patterns, illustrating the lattice volume change of SC-NC80 and SC-NM80 after charging to 4.4 V during the 1st cycle.

coin half cells with a traditional liquid electrolyte. During the 1st cycle, SC-NC80 and SC-NM80 deliver discharge capacities of 195 and 187 mAh g^{-1}, respectively (Fig. 2a). A higher capacity for SC-NC80 is expected since Co^{3+} is redox active while Mn^{4+} is not. However, as evidenced by the elevated voltage profile, SC-NM80 has a higher operating voltage than SC-NC80, which compensates for the lower discharge capacity in the energy density calculation. After 100 cycles at a C/3 rate, SC-NC80 and SC-NM80 retain 82% and 89%, respectively, of their initial C/3 discharge capacities (Fig. 2b). The improved cycling stability of SC-NM80 can be attributed to the inactive Mn^{4+} reinforcing the layered structure and the lower delithiation degree compared to SC-NC80. Incremental capacity analysis in Fig. 2c and Fig. 2d reveals the typical H (hexagonal) 1 ⇌ M (monoclinic) ⇌ H2 ⇌ H3 phase transitions for both cathodes when cycled at 2.8 to 4.4 vs. Li/Li^+ (V_{Li}). However, SC-NC80 undergoes H1 ⇌ M phase transitions at an earlier voltage onset due to the enhanced kinetics in phase transition and lithium vacancy ordering.[37] In addition, the H2 ⇌ H3 phase transition is also more attenuated owing to the solid-solution behavior from 20% Co^{3+} incorporation. Despite this, SC-NC80 suffers from worse phase irreversibility, as evidenced by the large voltage shift and phase transition peak intensity reduction (Fig. 2c). In contrast, SC-NM80 demonstrates less voltage shift and retains most of its phase transitions (Fig. 2d). This suggests that SC-NM80 is more resilient to lattice distortion from the repeated phase transitions. In general, high-Ni cathodes cycling past the H2 ⇌ H3 phase transition suffers from lattice oxygen release and surface rock-salt formation, which lowers the accessible capacity from the H3 phase due to the rock-salt phase preventing the layered structure from contracting in the (003) direction.[38] In addition, bulk degradation from structural defects, such as edge dislocations and rotational stacking faults, are energetically favorable to form at high SOC, leading to intragranular cracking and AM loss.[39,40] The observed difference in cycling stability likely originates from a combination of these factors; a detailed post-mortem analysis is warranted to further elucidate the degradation mechanism of single-crystal cathodes.

Interestingly, although both cathodes are charged past the voltage corresponding to the H2 → H3 phase transition occurs (Fig. 2c and Fig. 2d), they did not experience rapid lattice collapse. The lattice volume of SC-NC80 exhibits a slightly smaller shrinkage compared to that of SC-NM80 after charging to 4.4 V (-1.8% vs. -2.3%), even though SC-NC80 is at a higher delithiation degree (Fig. 2e). This phenomenon is attributed to the more anisotropic nature of SC-NC80, where its *c* lattice expands more than that of SC-NM80 during delithiation (2.7% vs. 1.4%).[27,41] Since the *a* lattice shrinkage is similar for both samples, the larger *c* lattice expansion reduces the overall volume change of SC-NC80. Overall, a 2% change in the cathode lattice volume is not significant enough to affect the intimate interfacial contact with the solid electrolyte in the cathode composite of ASSBs during cycling. Charging SC-NC80 and SC-NM80 beyond 4.5 V should be avoided to prevent the undesirable rapid lattice collapse and volume change that accelerate the capacity fade in ASSBs.

Kinetic characterization in conventional coin cells. Fig. 3 highlights the difference in the delithiation and lithiation kinetics of SC-NC80 and SC-NM80. Starting at a 5C rate, SC-NM80 becomes more sluggish during discharge compared to SC-NC80 (Fig. 3a). This is evident in the voltage profile of SC-NC80 (Fig. 3b) and SC-NM80 (Fig. 3c), where cell polarization becomes significant

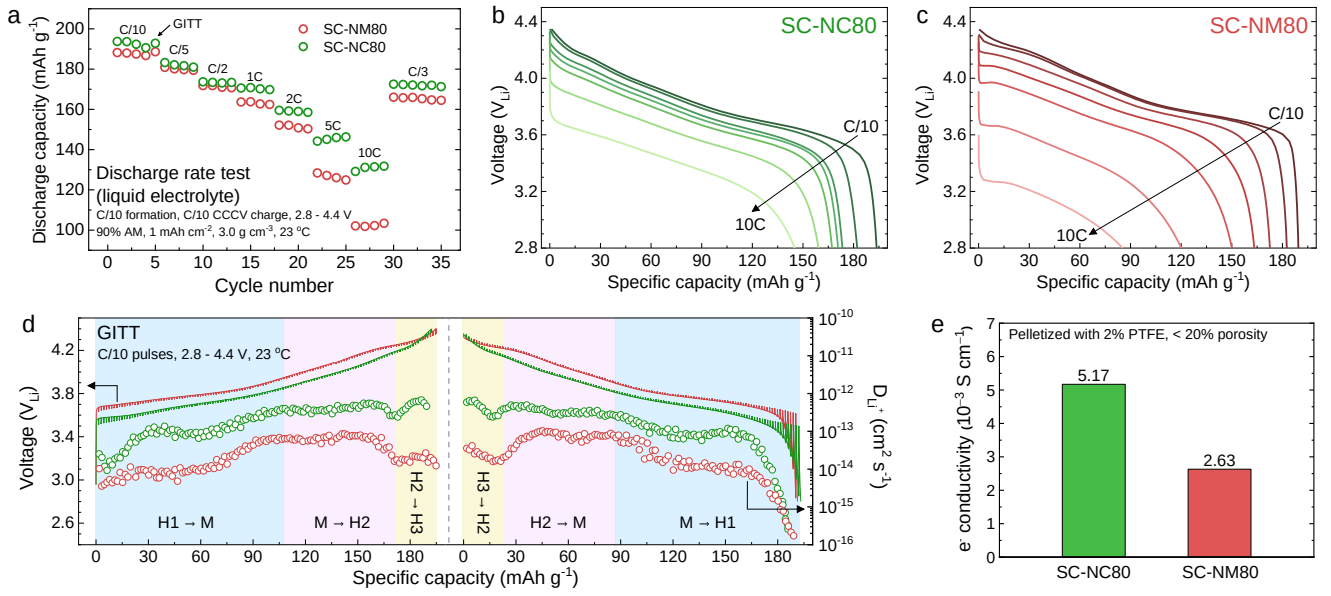

Fig. 3 Kinetic characterization of SC-NC80 and SC-NM80. (a) Discharge rate capability up to a 10C rate after charging at C/10. (b, c) Voltage profiles of (b) SC-NC80 and (c) SC-NM80 at different discharge rate. (d) GITT voltage profiles and the evolution of lithium diffusion coefficients (D_{Li^+}) for SC-NC80 and SC-NM80 during charge (left) and discharge (right). (e) Electronic conductivity of SC-NC80 and SC-NM80 determined by DC polarization.

starting at 5C for SC-NC80 and at 2C for SC-NM80. Particularly in the low voltage region coinciding with the M → H1 phase transition, the voltage profile begins to decline earlier at higher rates, indicating sluggish lithiation kinetics near the end of discharge. This effect is more pronounced for SC-NM80 and likely contributes to its reduced discharge capability.

To further delineate this phenomenon, the galvanostatic intermittent titration technique (GITT) is employed to measure the Li^+ diffusion coefficient (D_{Li^+}) of SC-NC80 and SC-NM80 (Fig. 3d). The overall D_{Li^+} of SC-NC80 is approximately an order of magnitude higher than that of SC-NM80 (~10^{-13} vs. ~10^{-14} cm^2 s^{-1}). This value aligns with the D_{Li^+} of single-crystalline $LiNiO_2$ and is generally lower than those of polycrystalline materials.[29,42] The reduced D_{Li^+} of SC-NM80 is attributed to the presence of Ni^{2+} in the Li^+ plane, hindering Li^+ diffusion.[43] D_{Li^+} generally increases during charge and decreases during discharge. However, during the H2 ⇌ H3 phase transitions, D_{Li^+} of SC-NM80 decreases and does not recover to the same level before the transition unlike that of SC-NC80. In addition, D_{Li^+} rapidly decreases by two to three orders of magnitude near the end of discharge, which can be ascribed to the difficulty for Li^+ to diffuse into a near fully lithiated layered structure. Evidently, SC-NM80 suffers more from poor lithiation kinetics at the low voltage region compared to SC-NC80, resulting in poor discharge rate capability. In addition to sluggish lithium diffusion kinetics, SC-NM80 also exhibits a lower electronic conductivity compared to SC-NC80 (2.63 x 10^{-3} vs. 5.17 x 10^{-3} S cm^{-1}, Fig. 3e and Fig. S5). Given that Co^{3+} is known to enhance cathode electronic conductivity and reduce Li/Ni mixing, it is unsurprising that SC-NC80 demonstrates superior lithium diffusion kinetics and electronic conductivity, leading to enhanced rate capability.[44] In summary, while SC-NM80 exhibits greater cycling stability, its rate capability lags behind SC-NC80 due to the reduced lithium diffusion kinetic and electronic conductivity.

Cycling performance in ASSBs. The optimized single-crystal cathodes are incorporated into dry electrodes to assess their electrochemical performances in ASSBs (Fig. 4). Fig. 4a illustrates the ASSB architecture utilized in this study, utilizing a dual solid-electrolyte strategy consisting of Li_3InCl_6 (LIC) as the cathode electrolyte and $Li_{5.5}PS_{4.5}Cl_{1.5}$ (LPSCl) as the separator (or anode electrolyte). This configuration ensures chemical and electrochemical stabilities with the single-crystal cathodes and $Li_{0.5}In$ alloy anode, respectively.[25,45–51] The dry cathode composite consists of 60 or 70 wt.% AM, 37 or 27 wt.% LIC, 2 wt.% VGCF as an electronically conductive agent, and 1 wt.% PTFE as a binder, with an areal loading of ~ 3 – 4 mAh cm^{-2}. A thin layer of LIC is situated between the cathode composite and the LPSCl separator layer to prevent oxidation of the unstable LPSCl separator layer. The use of a $Li_{0.5}In$ alloy help reduce anode instability issues associated with a Li-metal anode.[52] Coupled with a moderate current density at a C/3 rate (~ 1 mA cm^{-2}), this ASSB setup can effectively reveal any cathode degradation influencing the electrochemical result.[53]

Fig. 4b illustrates the cycling stability of SC-NC80 and SC-NM80 in ASSBs with 60% or 70% AM in the cathode composite. SC-NC80 exhibits a robust cycling stability over 200 cycles (~ 85% capacity retention) regardless of the AM fraction in the cathode composite. The overall cell polarization in 60% SC-NC80 is lower than that in 70% SC-NC80, likely due to a greater amount of LIC providing a uniform ionic coverage at the cathode interface. However, polarization growth is relatively higher for 60% SC-NC80 compared to 70% SC-NC80 after 200 cycles. With less AM fraction in the cathode composite, the ionic percolating network improves while the electronic percolating network reduces. Therefore, the greater polarization growth in 60% SC-NC80 likely stems from the loss of electrical contact. Interestingly, the cycling performance of SC-NM80 is perplexing. 60% SC-NM80 displays drastic dips in discharge capacity during cycling, which initially recover before dipping again without recovery. This phenomenon also occurs with 70% SC-NM80 to a much lesser extent and is fully recovered. The capacity retention of 70% SC-NM80 is much improved (~89%) compared to that of 60% SC-NM80 (~53%), even though they exhibit a similar overall cell polarization. Polarization growth is slightly more pronounced in 60% SC-NM80, which is similar to that observed in 60% SC-NC80. Since the main difference between 60% and 70% AM in the cathode composite is the coverage ratio between the solid electrolyte and the conductive carbon on cathode particles, the peculiar cycling behavior in SC-NM80 might be related to the electronic and ionic conductivity of the cathode composites.

Fig. 4c and Fig. S6 illustrate the effective electronic and ionic conductivity of the cathode composites containing 60% or 70% SC-NC80 or SC-NM80. Within the same AM fraction, the cathode composite with SC-NC80 has an order of magnitude higher electronic conductivity and only slightly higher ionic conductivity than the cathode composites with SC-NM80, which can be ascribed to the higher cathode electronic conductivity and lithium diffusion kinetics. When the AM fraction is increased, the electronic conductivity increases by two to threefold while the ionic conductivity decreases slightly. This can be rationalized by the reduced solid electrolyte volume sacrificing ionic contacts but allowing for better electrical contacts between the cathode particles and the conductive carbon matrix. More importantly, cathode composites with SC-NC80, regardless of AM fractions, exhibit higher electronic conductivities than ionic conductivities, while the converse is true for cathode composites with SC-NM80. This suggests that the mixed ionic-electronic conductivity of the cathode composite is a strong function of AM fraction and cathode composition. Incorporating Co-free cathodes with a lower electronic conductivity will reduce the electronic conductivity of the cathode composite, potentially accelerating capacity fade in ASSBs. Note that this effect is likely attenuated in this study

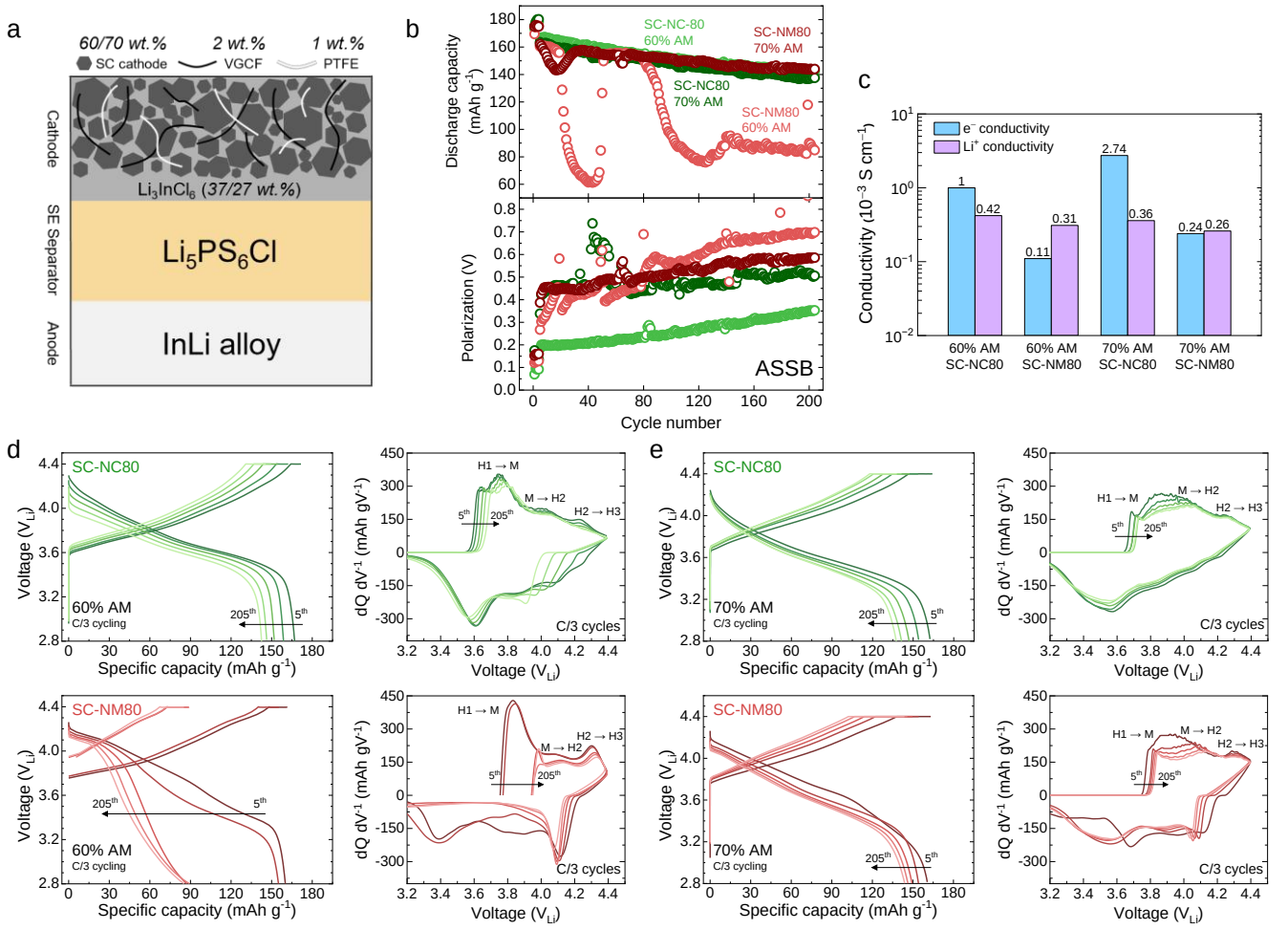

Fig. 4 Electrochemical characterization of SC-NC80 and SC-NM80 in ASSBs. (a) Schematic of the ASSB architecture depicting all the battery components. (b) Cycling performance (top) and polarization growth (bottom) of SC-NC80 and SC-NM80 with 60% or 70% AM in the cathode composite. (c) Electronic and ionic conductivity of various cathode composites containing 60% or 70% of SC-NC80 or SC-NM80. (d, e) Voltage profiles (left) and the corresponding dQ dV^{-1} curves (right) of SC-NC80 and SC-NM80 with (d) 60% or (e) 70% AM in the cathode composite during C/3 cycling.

since conductive carbon (VGCF) is used in the cathode composite.

Fig. 4d and Fig. 4e present the voltage profiles of the cathode composites containing 60% or 70%, respectively, of SC-NC80 or SC-NM80 during C/3 cycling, revealing how the mixed ionic-electronic conductivity of the cathode composite influences the electrochemical behavior of ASSBs. Both 60% and 70% SC-NC80 exhibit the typical voltage profiles similar to those observed in coin cell testing. However, 60% SC-NC80 displays a greater voltage drop compared to 70% SC-NC80 due to polarization growth after 200 cycles, consistent with the findings in Fig. 4b. Moreover, the peak features in dQ dV^{-1} are more distinct in 60% SC-NC80 due to the lower overall cell polarization. Although the polarization growth is lower in 70% SC-NC80, the voltage profile and the peak features in dQ dV^{-1} are merged and harder to distinguish, likely due to the higher overall cell polarization from the reduced solid electrolyte volume fraction. Despite this, 70% SC-NC80 has a capacity fade similar to that of 60% SC-NC80, suggesting that the cycling stability of SC-NC80 in ASSBs is not as sensitive to the electrode composition.

On the contrary, the voltage profiles of SC-NM80 deviate from those in coin cell testing, particularly in 60% SC-NM80. While the initial charge/discharge curves at the 5th cycle appear normal, a noticeable difference arises in the discharge curve below 4 V beginning at the 55th cycle. This divergence is more apparent in the dQ dV^{-1} plot, where a significant portion of the capacity in the reduction curve between 3.6 to 4 V is missing and shifted to below 3.6 V compared to the 5th cycle. By the 105th cycle, a substantial capacity below 4 V disappears during discharge, despite the majority of H2 ⇌ H3 phase transitions remaining electrochemically active. This suggests that the deactivation of SC-NM80 is SOC-dependent and is particularly pronounced at the low-voltage region, coinciding with H2 → M and M → H1 phase transitions. When the AM fraction is increased to 70%, the voltage profiles of 70% SC-NM80 become less anomalous, except for the 5th cycle, where some discharge capacity at around 3.6 V is shifted towards a lower voltage. This corresponds to the beginning of the peculiar capacity dipping

behavior during cycle life testing, which recovers after the 35th cycle (Fig. 4b). From this point on, the voltage profiles resemble those in coin cell testing, with only a small amount of discharge capacity originating from the M → H1 phase transition shifting towards a lower voltage.

Overall, the voltage and the dQ dV^{-1} curves provide intriguing insights into the abnormal electrochemical behavior of SC-NM80 in ASSBs and its relationship with the effective electronic and ionic conductivity of the cathode composite. As summarized in Fig. 4c, the electronic conductivity of cathode composites containing 60% or 70% SC-NM80 is lower than the ionic conductivity. Such imbalance leads to lithiation inhomogeneity across the thickness of the cathode composite during high-rate operation.[54] Due to sluggish electron transport, lithiation initially occurs near the current collector and propagates towards the separator. This lithiation gradient is exacerbated due to a lowered effective electronic conductivity when the AM fraction is reduced, hence 60% SC-NM80 experiences severe lithiation inhomogeneity.[55] Furthermore, the cathode mixed ionic-electronic conductivity generally increases as a function of SOC, which in turn alters the effective electronic and ionic conductivity of the cathode composite. The enhanced lithium diffusion kinetic is evident in Fig. 3d, where D_{Li^+} for SC-NM80 is the highest and plateaus in the medium SOC region near 4 V coinciding with the M ⇌ H2 phase transition. The cathode electronic conductivity is also increased by at least an order of magnitude due to the oxidation of $Ni^{2+/3+}$ to $Ni^{3+/4+}$ and the increased covalency of the Ni – O bonds.[56] The increase in effective electronic conductivity in the cathode composite is likely higher than the effective ionic conductivity.[57]

During lithiation (discharge), the converse is true – the mixed ionic-electronic conductivity of the cathode decreases. This is potentially the reason why the majority of the H2 ⇌ H3 phase transition in 60% SC-NM80 is retained while most of the capacity in the low voltage region is lost during discharge. The electronic conductivity during the H2 ⇌ H3 phase transition is higher than that in the low-voltage region, which enables sufficient electronic conduction throughout the entire cathode composite. The low-voltage region is not only sluggish in lithium diffusion (Fig. 3d), but also has the highest fraction of $Ni^{2+/3+}$ and thus the lowest cathode electronic conductivity. Hence, the effective electronic conductivity of 60% SC-NM80 would be the lowest near the end-of-discharge, further exacerbating the lithiation inhomogeneity in the cathode composite. All in all, the low cathode electronic conductivity of SC-NM80 results in a reduced effective electronic conductivity in 60% SC-NM80 cathode composite. This phenomenon promotes significant lithiation inhomogeneity, particularly in the low SOC region, even at a moderate cycling rate. Consequently, this leads to AM deactivation and eventual capacity loss in ASSBs. Increasing AM fraction above 70% is necessary to increase the effective electronic conductivity of the cathode composite and reduce lithiation inhomogeneity. Furthermore, incorporation of conductive additives, such as carbon black or Ti_2O_3, along with a rational mixing sequence of electrode components, can further promote sufficient electronic percolation within the cathode composite.[58,59]

Conclusions

By comparing the materials properties and the electrochemical behaviors of SC-NC80 and SC-NM80 in both conventional LIBs and ASSBs, it was demonstrated that the lower electronic conductivity of SC-NM80 presents technical challenges for its integration into ASSBs. Cathode composites containing SC-NM80 generally exhibit lower electronic conductivities than ionic conductivities, leading to lithiation inhomogeneity during cycling. Such inhomogeneity is the most severe when the AM fraction is low, with its impact on capacity loss most prominent in the low SOC region. In contrast, SC-NC80 can be effectively integrated in ASSBs with a low sensitivity to AM fraction in the cathode composite because the effective electronic conductivity of the cathode composite benefits from the higher cathode electronic conductivity. This study highlights how the cathode mixed ionic-electronic conductivity influences the electrode conductivity of the cathode composite and thus the cycling stability of ASSBs. While removing cobalt in high-Ni cathodes is feasible in traditional LIBs with a liquid electrolyte, implementing Co-free cathodes in ASSBs requires robust electrode engineering to optimize electronic conduction pathways within the cathode composite and enable high-rate cycling without compromising cycle life due to reaction inhomogeneity.

Conflicts of interest

The authors declare the following competing financial interest(s): Arumugam Manthiram is a co-founder of TexPower, a startup company focusing on cobalt-free cathode materials for lithium-ion batteries.

Acknowledgements

This work was supported by the Assistant Secretary for Energy Efficiency and Renewable Energy, Office of Vehicle Technologies of the U.S. Department of Energy through the Advanced Battery Materials Research (BMR) Program (Battery500 Consortium) award number DE-AC05-76RLO1830 and the Welch Foundation grant F-1254.

Notes and references

1 S. Lee and A. Manthiram, *ACS Energy Lett.*, 2022, **7**, 3058–3063.
2 W. Li, S. Lee and A. Manthiram, *Adv. Mater.*, 2020, **32**, 2002718.
3 M. Yi, W. Li and A. Manthiram, *Chem. Mater.*, 2022, **34**, 629–642.
4 T. Liu, L. Yu, J. Liu, J. Lu, X. Bi, A. Dai, M. Li, M. Li, Z. Hu, L. Ma, D. Luo, J. Zheng, T. Wu, Y. Ren, J. Wen, F. Pan and K. Amine, *Nat. Energy*, 2021, **6**, 277–286.

5 Z. Cui, Q. Xie and A. Manthiram, *Adv. Energy Mater.*, 2021, **11**, 2102421.
6 L. Mu, R. Zhang, W. H. Kan, Y. Zhang, L. Li, C. Kuai, B. Zydlewski, M. M. Rahman, C. Sun, S. Sainio, M. Avdeev, D. Nordlund, H. L. Xin and F. Lin, *Chem. Mater.*, 2019, **31**, 9769–9776.
7 L. Mu, W. H. Kan, C. Kuai, Z. Yang, L. Li, C. Sun, S. Sainio, M. Avdeev, D. Nordlund and F. Lin, *ACS Appl. Mater. Interfaces*, 2020, **12**, 12874–12882.
8 H. Li, M. Cormier, N. Zhang, J. Inglis, J. Li and J. R. Dahn, *J. Electrochem. Soc.*, 2019, **166**, A429–A439.
9 W. Li, B. Song and A. Manthiram, *Chem. Soc. Rev.*, 2017, **46**, 3006–3059.
10 A. Tornheim, S. Sharifi-Asl, J. C. Garcia, J. Bareño, H. Iddir, R. Shahbazian-Yassar and Z. Zhang, *Nano Energy*, 2019, **55**, 216–225.
11 B. Strehle, F. Friedrich and H. A. Gasteiger, *J. Electrochem. Soc.*, 2021, **168**, 050512.
12 J. Langdon and A. Manthiram, *Energy Storage Mater.*, 2021, **37**, 143–160.
13 G. Qian, Y. Zhang, L. Li, R. Zhang, J. Xu, Z. Cheng, S. Xie, H. Wang, Q. Rao, Y. He, Y. Shen, L. Chen, M. Tang and Z. F. Ma, *Energy Storage Mater.*, 2020, **27**, 140–149.
14 H. Li, J. Li, X. Ma and J. R. Dahn, *J. Electrochem. Soc.*, 2018, **165**, 1038–1045.
15 J. Li, A. R. Cameron, H. Li, S. Glazier, D. Xiong, M. Chatzidakis, J. Allen, G. A. Botton and J. R. Dahn, *J. Electrochem. Soc.*, 2017, **164**, A1534–A1544.
16 S. Oswald, D. Pritzl, M. Wetjen and H. A. Gasteiger, *J. Electrochem. Soc.*, 2021, **168**, 120501.
17 S. Lee, L. Su, A. Mesnier, Z. Cui and A. Manthiram, *Joule*, 2023, **7**, 2430–2444.
18 E. Trevisanello, R. Ruess, G. Conforto, F. H. Richter and J. Janek, *Adv. Energy Mater.*, 2021, **11**, 2003400.
19 D. Lee, A. Mesnier and A. Manthiram, *Adv. Energy Mater.*, 2024, **14**, 2303490.
20 S. Randau, D. A. Weber, O. Kötz, R. Koerver, P. Braun, A. Weber, E. Ivers-Tiffée, T. Adermann, J. Kulisch, W. G. Zeier, F. H. Richter and J. Janek, *Nat. Energy*, 2020, **5**, 259–270.
21 J. Schnell, T. Günther, T. Knoche, C. Vieider, L. Köhler, A. Just, M. Keller, S. Passerini and G. Reinhart, *J Power Sources*, 2018, **382**, 160–175.
22 W. Li, H. Y. Asl, Q. Xie and A. Manthiram, *J. Am. Chem. Soc.*, 2019, **141**, 5097–5101.
23 H. Li, A. Liu, N. Zhang, Y. Wang, S. Yin, H. Wu and J. R. Dahn, *Chem. Mater.*, 2019, **31**, 7574–7583.
24 G. Conforto, R. Ruess, D. Schröder, E. Trevisanello, R. Fantin, F. H. Richter and J. Janek, *J Electrochem Soc*, 2021, **168**, 070546.
25 Y. Han, S. H. Jung, H. Kwak, S. Jun, H. H. Kwak, J. H. Lee, S. T. Hong and Y. S. Jung, *Adv. Energy Mater.*, 2021, **11**, 2100126.
26 C. Wang, R. Yu, S. Hwang, J. Liang, X. Li, C. Zhao, Y. Sun, J. Wang, N. Holmes, R. Li, H. Huang, S. Zhao, L. Zhang, S. Lu, D. Su and X. Sun, *Energy Storage Mater.*, 2020, **30**, 98–103.
27 D. Goonetilleke, F. Riewald, A. O. Kondrakov, J. Janek, T. Brezesinski and M. Bianchini, *J. Phys. Chem. C*, 2022, **126**, 16952–16964.
28 S. Lee, C. Li and A. Manthiram, *Adv. Energy Mater.*, 2024, 2400662.
29 Y. C. Chien, H. Liu, A. S. Menon, W. R. Brant, D. Brandell and M. J. Lacey, *Nat. Commun.*, 2023, **14**, 2289.
30 Z. Siroma, T. Sato, T. Takeuchi, R. Nagai, A. Ota and T. Ioroi, *J. Power Sources*, 2016, **316**, 215–223.
31 Y. Bi, J. Tao, Y. Wu, L. Li, Y. Xu, E. Hu, B. Wu, J. Hu, C. Wang, J. G. Zhang, Y. Qi and J. Xiao, *Science (1979)*, 2020, **370**, 1313–1318.
32 F. Strauss, T. Bartsch, L. De Biasi, A.-Y. Kim, J. Janek, P. Hartmann and T. Brezesinski, *ACS Energy Lett.*, 2018, **3**, 992–996.
33 P. Yan, J. Zheng, J. Zheng, Z. Wang, G. Teng, S. Kuppan, J. Xiao, G. Chen, F. Pan, J. G. Zhang and C. M. Wang, *Adv. Energy Mater.*, 2016, **6**, 1502455.
34 Y. Kim, *ACS Appl. Mater. Interfaces*, 2012, **4**, 2329–2333.
35 A. Rougier, I. Saadoune, P. Gravereau, P. Willmann and C. Delmas, *Solid State Ion.*, 1996, **90**, 83–90.
36 D. Wang, C. Xin, M. Zhang, J. Bai, J. Zheng, R. Kou, Y. Xiao, K. Amine, F. Pan and F. Wang, *Chem. Mater.*, 2019, **31**, 2731–2740.
37 C. Xu, P. J. Reeves, Q. Jacquet and C. P. Grey, *Adv. Energy Mater.*, 2021, **11**, 2003404.
38 C. Xu, K. Märker, J. Lee, A. Mahadevegowda, P. J. Reeves, S. J. Day, M. F. Groh, S. P. Emge, C. Ducati, B. L. Mehdi, C. C. Tang and C. P. Grey, *Nat. Mater.*, 2021, **20**, 84–92.
39 P. Yan, J. Zheng, M. Gu, J. Xiao, J. G. Zhang and C. M. Wang, *Nat. Commun.*, 2017, **8**, 14101.
40 D. Eum, S. O. Park, H. Y. Jang, Y. Jeon, J. H. Song, S. Han, K. Kim and K. Kang, *Nat. Mater.*
41 T. Liu, L. Yu, J. Lu, T. Zhou, X. Huang, Z. Cai, A. Dai, J. Gim, Y. Ren, X. Xiao, M. V. Holt, Y. S. Chu, I. Arslan, J. Wen and K. Amine, *Nat. Commun.*, 2021, **12**, 6024.
42 A. Mesnier and A. Manthiram, *J. Electrochem. Soc.*, 2023, **170**, 080509.
43 J. Choi and A. Manthiram, *Solid State Ion.*, 2005, **176**, 2251–2256.
44 A. Manthiram, *Nat. Commun.*, 2020, **11**, 1550.
45 T. Asano, A. Sakai, S. Ouchi, M. Sakaida, A. Miyazaki and S. Hasegawa, *Adv. Mater.*, 2018, **30**, 1803075.
46 L. M. Riegger, R. Schlem, J. Sann, W. G. Zeier and J. Janek, *Angew. Chem. Int. Ed.*, 2021, **60**, 6718–6723.
47 S. Wenzel, D. A. Weber, T. Leichtweiss, M. R. Busche, J. Sann and J. Janek, *Solid State Ion.*, 2016, **286**, 24–33.
48 R. Koerver, I. Aygün, T. Leichtweiß, C. Dietrich, W. Zhang, J. O. Binder, P. Hartmann, W. G. Zeier and J. Janek, *Chem. Mater.*, 2017, **29**, 5574–5582.
49 X. Li, J. Liang, X. Yang, K. R. Adair, C. Wang, F. Zhao and X. Sun, *Energy Environ. Sci.*, 2020, **13**, 1429–1461.
50 J. Auvergniot, A. Cassel, J. B. Ledeuil, V. Viallet, V. Seznec and R. Dedryvère, *Chem. Mater.*, 2017, **29**, 3883–3890.
51 A. Banerjee, H. Tang, X. Wang, J. H. Cheng, H. Nguyen, M. Zhang, D. H. S. Tan, T. A. Wynn, E. A. Wu, J. M. Doux, T. Wu, L. Ma, G. E. Sterbinsky, M. S. D'Souza, S. P. Ong and Y. S. Meng, *ACS Appl Mater. Interfaces*, 2019, **11**, 43138–43145.
52 M. Nagao, A. Hayashi and M. Tatsumisago, *Electrochemistry*, 2012, **80**, 734–736.
53 S. Luo, Z. Wang, X. Li, X. Liu, H. Wang, W. Ma, L. Zhang, L. Zhu and X. Zhang, *Nat. Commun.*, 2021, **12**, 6968.
54 K. G. Naik, B. S. Vishnugopi and P. P. Mukherjee, *Energy Storage Mater.*, 2023, **55**, 312–321.
55 A. M. Stavola, X. Sun, D. P. Guida, A. M. Bruck, D. Cao, J. S. Okasinski, A. C. Chuang, H. Zhu and J. W. Gallaway, *ACS Energy Lett.*, 2023, **8**, 1273–1280.
56 R. Amin and Y.-M. Chiang, *J. Electrochem. Soc.*, 2016, **163**, A1512–A1517.
57 T. Asano, S. Yubuchi, A. Sakuda, A. Hayashi and M. Tatsumisago, *J. Electrochem. Soc.*, 2017, **164**, A3960–A3963.

58 R. Fang, Y. Liu, Y. Li, A. Manthiram and J. B. Goodenough, *Mater. Today*, 2023, **64**, 52–60.

59 S. Noh, W. T. Nichols, M. Cho and D. Shin, *J Electroceram*, 2018, **40**, 293–299.

Data Availability Statement

The datasets generated and/or analyzed during the current study are available from the authors on reasonable request.